Article

Not peer-reviewed version

Analysis of Fatigue Property of the Aviation Gear Steel 15Cr14Co12Mo5Ni2 During High-Temperature Carburizing and Quenching

Wei Feng * , Yifan Zhou , Yuhao Zhang , Ruikun Wang , Xinhao Zhao *

Posted Date: 17 April 2026

doi: 10.20944/preprints202604.1274.v1

Keywords: 15Cr14Co12Mo5Ni2 aviation gear steel; quenching temperature; axial tesioncompressive fatigue; fatigue life

Preprints.org (www.preprints.org) | NOT PEER-REVIEWED | Posted: 17 April 2026 doi:10.20944/preprints202604.1274.v1

Article

Analysis of Fatigue Property of the Aviation Gear Steel 15Cr14Co12Mo5Ni2 During High-Temperature Carburizing and Quenching

Wei Feng [1,2,3,*], Yifan Zhou [1],Yuhao Zhang [1], Ruikun Wang [1] and Xinhao Zhao [3,*]

[1] School of Materials Science and Engineering, Wuhan University of Technology, Wuhan 430070, China
[2] State Key Laboratory of Light Superalloys, Wuhan University of Technology, Wuhan 430070, China
[3] AECC Zhongchuan Transmission Machinery Co., Ltd., Changsha 410000, China
* Correspondence: fengwei@whut,edu.cn (W.F.); zhaoxh729@foxmail.com (X.Z.)

Abstract

15Cr14Co12Mo5Ni2, as a new type of low-carbon high-alloy aviation gear steel, has shown significant application potential in the transmission systems of aero engines due to its excellent high-temperature performance. In this paper, the aviation gear steel 15Cr14Co12Mo5Ni2 was treated by carburizing and quenching process. The microstructure distributions of the carburized and quenched aviation gear steel at different quenching temperature were analyzed by OM, SEM and EBSD. Subsequently, the axial tension-compressive fatigue tests (stress ratio R=-1) were carried out using a high-frequency fatigue testing machine after heat treatment at different quenching temperature (1020 ° C, 1050 ° C and 1080 ° C), and the stress-number of cycles (S-N) curves were obtained by fitting the number of fatigue fracture cycles. The fracture morphologies were observed by SEM and the fracture mechanisms were analyzed. The research results show that the distribution of the microstructure and carbides exhibit gradient characteristics, and the carbide content decreases and the effective carburized layer depth decreases from 0.65mm to 0.45mm with increasing quenching temperature, also the main carbide types are $M_{23}C_6$ and M_7C_3. The fatigue life of 15Cr14Co12Mo5Ni2 gear steel decreases as the quenching temperature increases. Their fatigue strengths at a given fatigue life of 10^6 cycles at 1020 °C, 1050 °C and 1080 °C are 192 MPa, 183 MPa and 158 MPa, respectively. The cracks propagate outward from the core and the propagation rate accelerates with the increasing quenching temperature, eventually fracturing in the carburized layer. The fracture mechanism of 15Cr14Co12Mo5Ni2 gear steel at the quenching temperatures of 1020 °C was a mixed mode of intergranular and cleavage brittle fracture, while at 1050 °Cand 1080 °C, it is mainly brittle fracture accompanied by local ductile fracture.

Keywords: 15Cr14Co12Mo5Ni2 aviation gear steel; quenching temperature; axial tesion-compressive fatigue; fatigue life

1. Introduction

Aviation gears typically operate in extreme service environments such as high speeds, elevated temperatures, and alternating heavy loads, and are required to possess high load-bearing capacity and fatigue resistance to ensure the normal operation of aero engines and the safe flight of airplanes [1]. In most cases, fatigue failure is the main failure mode of aviation gears. Fatigue failure occurs when the stress level is far lower than the static tensile strength of the material and suddenly leads to fracture after a sufficient number of cycles, which is characterized by its concealment and often results in catastrophic consequences. Therefore, fatigue failure has become a persistent core challenge due to its inherent complexity and unpredictable feature in engineering design and materials science, especially for aviation gear components and materials serving in extreme environments [2].

Fatigue performance is not an intrinsic material property, but rather a characteristic that exhibits high sensitivity to microstructure variations such as grain type, size, distribution, and so on [3–5]. This characteristic provides a basis for actively regulating the microstructure to improve the fatigue strength, hence enhancing the service life of components. Among available methods for controlling microstructure, heat treatment plays a crucial role in shaping the final performance of materials. Studies have shown that rational design of heat treatment parameters can effectively enhance the fatigue resistance of materials [6–9]. Surface hardening treatments techniques, such as carburizing, nitriding and induction hardening, are widely used to low carbon alloy steels by changing the surface structure and stress state to improve their fatigue resistance [10–14]. Quenching is a fundamental heat treatment process that significantly enhances the mechanical properties of materials by generating metastable, non-equilibrium microstructures. During quenching process, the quenching temperature acts as the governing parameter, functioning as a precise initiator for microstructural evolution, phase transformations, dissolution and precipitation of alloying elements and residual stress and deformation, which regulates the material's hardness, strength and resultant toughness. However, the relationship between strength and fatigue performance is not an oversimplified positive correlation. An increase in quenching temperature can enhance the hardness and strength of materials, but its fatigue strength will decrease [15,16].

In the heat treatment process of alloy steel, the heating temperature directly determines the austenitizing process which significantly affects the grain size of austenite, the solubility of carbides carbon and alloy elements, and their distribution in matrix, thus influencing the mechanical properties. During heating 52100 bearing steel, Li et al. [17] found that increasing the austenitization temperature will reduce the volume fraction of undissolved carbides and increase the carbon content, thus lead to the conflict between hardness and toughness. It was found that the grain size of austenite increases from 25.4μm to 52.8μm when the quenching temperature increases from 1150 °C to 1250 °C during the austenitizing treatment of 700 MPa grade high-strength steel [18]. Increasing the austenitizing temperature above 1050 °C promotes the dissolution of coarse M23C6-type carbides during heat treatment of 10Cr12Ni3Mo2VN steel, resulting in improved low-temperature toughness [19]. When the quenching temperature is too low, the austenitization is incomplete, and the carbonides are not fully dissolved, resulting in the formation of the undissolved hard phase, which becomes a crack source for the early initiation of fatigue cracks. When the quenching temperature is too high, the austenite grains will undergo rapid coarsening, thus reducing the material's strength.

By choosing an appropriate quenching temperature for metallic materials, a finer ferrite structure or martensite-bainite multiphase structure can be obtained, and dislocation slip can also be delayed, thereby enhancing the fatigue performance of the material [15,20]. This because that bainite can modulate the strength and toughness balance of the material, and higher toughness is conducive to hinder the propagation of microcracks, thereby potentially improving fatigue performance [21]. Additionally, some research indicates that quenching temperature will affect the content and stability of residual austenite for the quenched steel sample. As we all know that the retained austenite was metastable and the stability of its mechanical properties will change with temperature variations, and it will partially or completely transform into a martensitic structure under strain-induced action [22,23]. Appropriate and uniformly distributed residual austenite is conducive to the good fatigue performance of material, due to the transformation of RA will be beneficial to reduce the rate of crack propagation [24]. For low-carbon steel that has undergone carburizing and quenching treatment, the transformation of retained austenite into martensite will lead to instability and anisotropy of residual stress during cyclic loading, thereby affecting the fatigue performance of the material [25]. Excessive or unstable residual austenite may prematurely transform under cyclic stress, instead introducing microcracks or causing dimensional instability. Meanwhile, the quenching temperature directly determines the residual stress state within the material after quenching and cooling. After quenching and tempering treatment of high-carbon 52100 steel, the higher initial amounts of retained austenite will improve fatigue crack growth resistance, and inhibit brittle intergranular fracture and promote transgranular fracture. This might be due to the transformation of RA near crack propagation will intensify the compressive stress at the crack tip and form microcracks at the untempered martensite interface [26].The surface residual compressive stress is recognized as a favorable factor that can effectively close fatigue cracks and enhance fatigue strength (especially high-cycle fatigue)[27–29].

15Cr14Co12Mo5Ni2 is a new generation of low-carbon and high-alloy aviation gear steel. By determining the appropriate carburizing and quenching heat treatment process, the alloy can obtain high surface hardness and better core fracture toughness and impact resistance, which can meet the high temperature, high load and impact working conditions of aero engines [30]. At present, several scholars have studied its high-temperature fatigue strength after carburizing and quenching treatment [31], as well as the evolution mechanism of microstructure and mechanical properties after cold forging forming [32]. However, no literature has reported the influence of quenching temperature on the fatigue behavior of this alloy yet.

In the present work, the vacuum carburizing and high-temperature quenching heat treatment process were carried out on 15Cr14Co12Mo5Ni2 aviation gear steel. To understand and evaluate the effect of quenching temperature on fatigue resistance, the axial tension-compressive fatigue tests were performed on a high-frequency fatigue testing machine at different quenching temperature (1020 °C, 1050 °C and 1080 °C). The stress-number of cycles (S-N) curves were obtained by fitting the fatigue test data. The fracture morphologies were observed by SEM and the fracture mechanism was analyzed. This research can provide theoretical basis and experimental support for the process parameter optimization of 15Cr14Co12Mo5Ni2 steel in the manufacturing of high-performance and long-life aviation gears.

2. Materials and Methods

2.1. Material Preparation and Heat Treatment Process

The aviation gear steel 15Cr14Co12Mo5Ni2 ingot used in this work was smelted by the vacuum induction melting + vacuum arc remelting (VIM+VAR) method and forged into round bars, and its main chemical composition is shown in Table .

Table 1. Cr14Co12Mo5Ni2W Steel Chemical Composition (wt.%).

C	Cr	Co	Mo	Ni	W	V	Fe
0.13	13.89	12.49	4.61	1.99	0.62	0.61	Bal

Three aviation gear steel plate samples with a length of 160mm, a width of 60mm and a thickness of 3mm were cut from a round bar annealed along a direction parallel to the rolling direction for heat treatment experiments, as shown in Figure 1a. Then the plate samples were performed heat treatment according to the process as shown in Figure 2 [33]. The heat treatment process can be divided into two parts. The first part is the carburizing and high-temperature tempering stage: The vacuum carburizing furnace was first heated to 800 °C with holding timewas of 30 minutes. Then, the temperature rises up to 950 °C holding for 20 minutes for high-temperature pre-oxidation. Subsequently, carburizing was carried out at 960 °C under different carbon potentials (1.15%, 1.05% and 0.8%, respectively) for 7 hours, followed by air cooling; and then, high-temperature tempering was carried out at 593 °C for 240 minutes and air cooling, as illustrated in Figure 2a. After carburizing in vacuum furnace, the quenching and tempering stage was performed: three plate samples were heated at 1020 °C, 1050 °C, and 1080 °C respectively for 45min and then quenched by oil, followed by tempering at 500 °C for 2 h, air cooling, finally by supplementary tempering at 500 °C for 2 h , air cooling, as shown in Figure 2b.

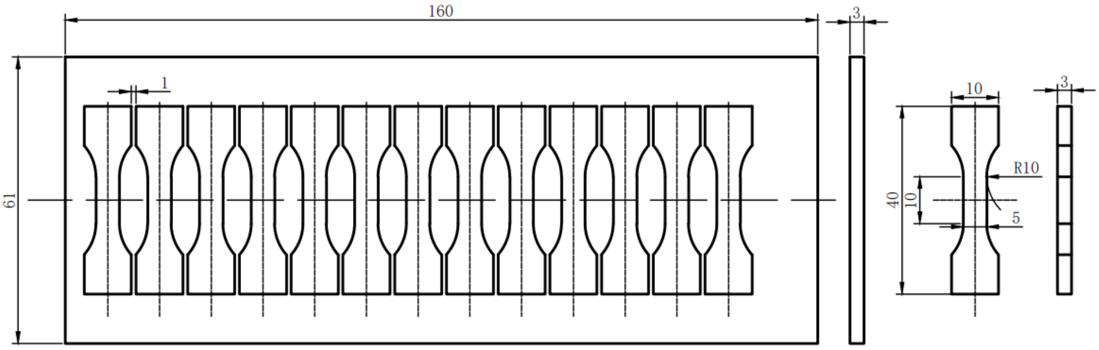

(a) (b)

Figure 1. Sample diagram. (a) heat-treated sample; (b) Fatigue test specimens (unit: mm).

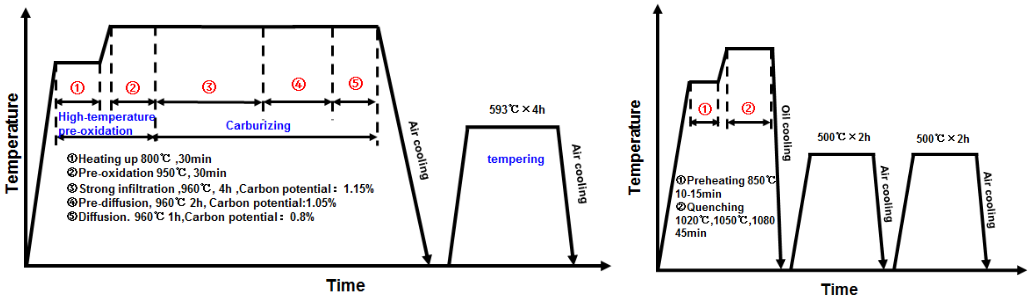

(**a**) (**b**)

Figure 2. Schematic diagram of heat treatment process: (a) carburizing and high-temperature tempering stage; (b) quenching and tempering stage.

2.2. Fatigue Experiments

Twelve fatigue samples were taken from each steel plate treated at different quenching temperatures at intervals of 1mm, as shown in Figure 1a. The specimen shape and specific dimensions with a gauge length of 10 mm are illustrated in Figure 1b. The tension-compression fatigue test was conducted on the QBG-100LN high-frequency fatigue testing machine, as shown in Figure 3a. The cyclic load F was applied along the centerline of the sample to simulate the stress state under working conditions, as depicted in Figure 3b. A constant stress ratio of R =-1 was used, and the loading amplitude was controlled by applying a sine waveform with a frequency of 70 Hz. To obtain the Stress versus Cycles to failure (S-N) curve, cyclic load F can be calculated by adjusting the stress amplitude according to Eqaution (1):

$$F = \sigma * B * H, \quad (1)$$

where, σ represents the stress amplitude. B is the sample width, which is 10mm, and H represents the sample thickness, which is 3mm.

In this experiment, the stress level is set to be related to the yield strength σ0 of the aviation gear steel, that is 0.8σ0, 0.6σ0, 0.4σ0, and 0.2σ0, respectively. In the previous tests, the yield strength σ0 was measured to be 1016 MPa [32]. Therefore, during fatigue tests, the stress amplitudes are set to 812MPa, 609 MPa, 406 MPa and 203 MPa, respectively, and the samples are subjected to the cycle loading as shown in Figure 3c under different stress amplitudes. During fatigue tests, the run-out criterion is set to 10^6 cycles, which means the test will stop if the sample doesn't fail before the number of cycles exceeds 10^6 under the given stress. In order to ensure the accuracy of the experiment results, three repeated fatigue tests were performed at every stress level under different quenching temperature. The total number of specimens prepared is 36, and 36 fatigue tests were carried out.

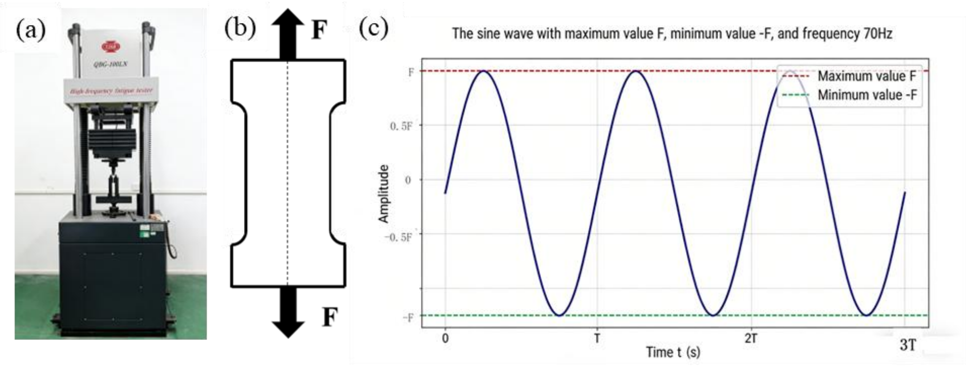

Figure 3. High-frequency fatigue testing machine.(a)The physical specimen of the testing machine;(b)Load model;(c)Load condition.

2.3. Microstructure Characterization

After the fatigue experiments, the fatigue fracture surfaces and the microstructures of the specimens after heat treatment at different quenching temperatures were observed and analyzed using an optical microscope (OM, IE500M, China), scanning electron microscope (SEM, JSM-IT800, JEOL,Japan) operated at 15kV, energy dispersive spectrometer (EDS, attached to the JSM-IT800) and electron back scattered diffraction (EBSD). EBSD analysis was performed using a Zeiss Gemini 300 (Carl Zeiss AG, Germany) field-emission scanning electron microscope equipped with an OxfordCanon EBSD system at an accelerating voltage of 20kV,with a scanning area of 32×24μm² and a step size of 0.05μm.Prior to OM and SEM observations, the specimens were ground in sequence by 80#, 800#, 1000# and 2000# SiC sandpapers, followed by polishing with a 2.5μm diamond suspension. Subsequently, the polished specimens were ultrasonically cleaned and then etched for approximately 2 min in a solution consisting of HCl, HNO3, CuCl2, FeCl3, H2O and anhydrous ethanol. Before EBSD examination, the specimens were further prepared using an IM4000plus argon ion polishing instrument through the voltage of 4kV, the incident angle of 3° for 2h in the first stage, followed by 2.5kV, 1.5° and 1.5h in the second stage.

2.4. Hardness Tests

The Vickers hardness of the heat-treated samples was measured by using the Huayin Micro Vickers hardness tester (HV-1000A, China). During the testing process, the starting position for hardness measurement was set at a distance of 0.05mm from the cross-section of the sample. The hardness test was conducted from the surface inward at intervals of 0.1mm along the rolled direction with a load of 200g for 10s. Three different positions were selected for hardness testing, and the average value of each measurement was taken to ensure the accuracy of Vickers hardness measurement.

3. Experimental Results and Discussion

3.1. Microstructure Characteristics

The optical micrographs of the aviation gear steel 15Cr14Co12Mo5Ni2 from the surface to the core at different quenching temperatures after carburizing and quenching treatment are illustrated in Figure 4. It can be observed that all the samples at the three temperatures present three typical regions: the outer high-carbon carburized zone, the middle low-carbon transition zone, and core zone without carbon enrichment in the center.

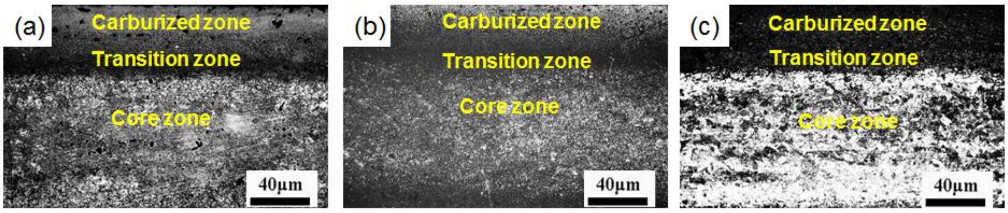

Figure 4. OM diagrams after heat treatment at different quenching temperatures: (a) 1020 °C; (b) 1050 °C; (b) 1080 °C.

Figure 5 shows the scanning electron microscope (SEM) morphologies of the carburized zone, transition zone and core zone of the sample at different quenching temperatures. From Figure 5(a1,b1,c1), it can be found that a large amount of carbides are observed in the carbide layer, and are mainly distributed in a continuous network and chain pattern along the grain boundaries as well as in granular form within the grains at all quenching temperatures. In the transition zone, the carbides are fine in size and dispersed in the matrix at the quenching temperature of 1020 °C; The amount of carbides decreases, but their distribution pattern is similar to that of the carburized layer at the quenching temperature of 1050 °C; While at 1080 °C quenching, the carbides tend to coarsen and have irregular contours, as shown in Figure 5(a2,b2,c2). As seen from Figure 5(a3,b3,c3), the quenching temperature has a significant influence on the microstructure of core zone: at 1020 °C, a small amount of fine-sized carbide particles are dispersed in the matrix; at the quenching temperature of 1050 °C, two distinct microstructure regions are observed and lath martensites of different size and spacings are observed by high-magnification scanning electron microscope; at the quenching temperature of 1080 °C, only a small number of fine carbides remain, and the uniformity of the microstructure has been significantly improved.

In summary, as the quenching temperature increases, the solubility of carbides in austenite continuously increases, resulting in a gradient evolution of the carbon content, morphology, size, and spatial distribution of carbides from the surface to the core region.

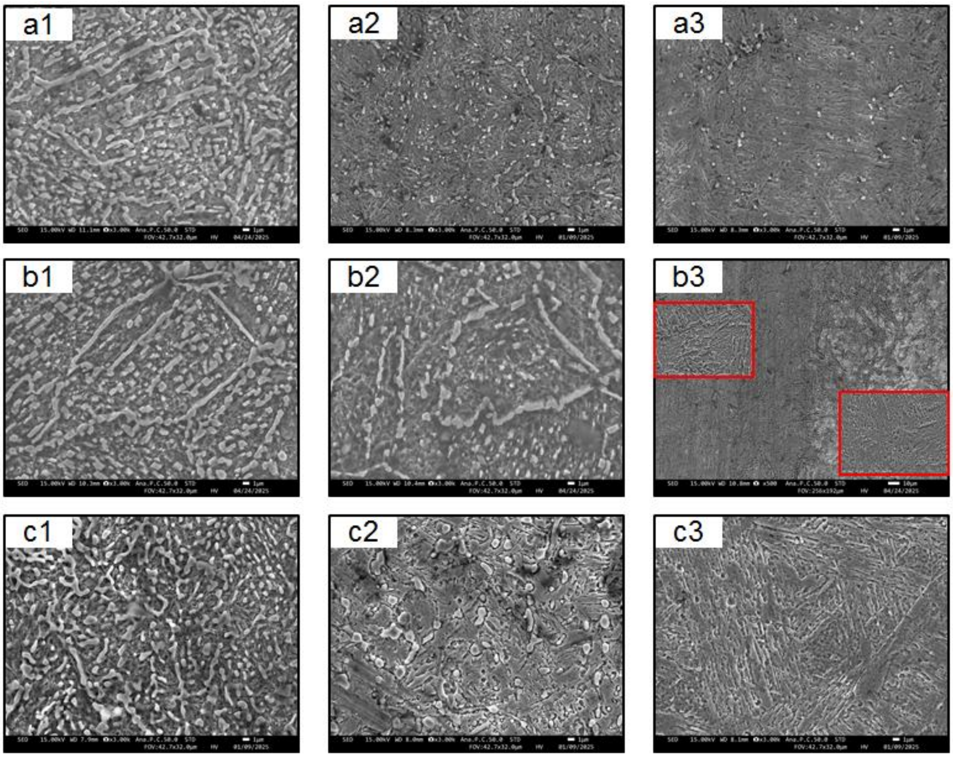

Figure 5. SEM images of the microstructure distribution in the carburized zone (a1-c1), transition zone (a2-c2) and core zone (a3-c3) of the sample at different quenching temperatures: (a) 1020 °C; (b) 1050 °C; (b) 1080 °C.

Figure 6 shows the EBSD phase distribution and grain boundary superposition diagrams of samples at different temperatures. Through the phase diagrams, the distribution and content of each phase in different regions at different temperatures can be determined.

It can be seen from Figure 6 that the matrix structure of the sample mainly transforms into a martensitic phase with a BCC structure after heat treatment. In the carburized zone, the main carbide types are $M_{23}C_6$ and M_7C_3, among which the content of M_7C_3 type carbides is relatively high and mainly distributed along the grain boundaries. The $M_{23}C_6$ type carbides have a relatively low content and are mainly distributed within the grain boundaries. In the transition zone, the carbon content decreases and the content of $M_{23}C_6$ type carbides increases, while the content of M_7C_3 decreases significantly. As the carbon content in the core zone further decreases, the matrix contains a small amount of $M_{23}C_6$ type carbides at the temperature of 1020 °C and 1050 °C.

Table 2 shows the content of each phase in different regions at different quenching temperatures. As can be seen in Table 2, the total content of carbides in the carburized layer gradually decreases with the increase of quenching temperature, among which M_7C_3 gradually decreases and $M_{23}C_6$ gradually increases. The content of martensite increases with the rise in temperature and the grains are coarser. It can also be known from Table 2 that there is a very small amount of residual austenite (RA) in the matrix after heat treatment.

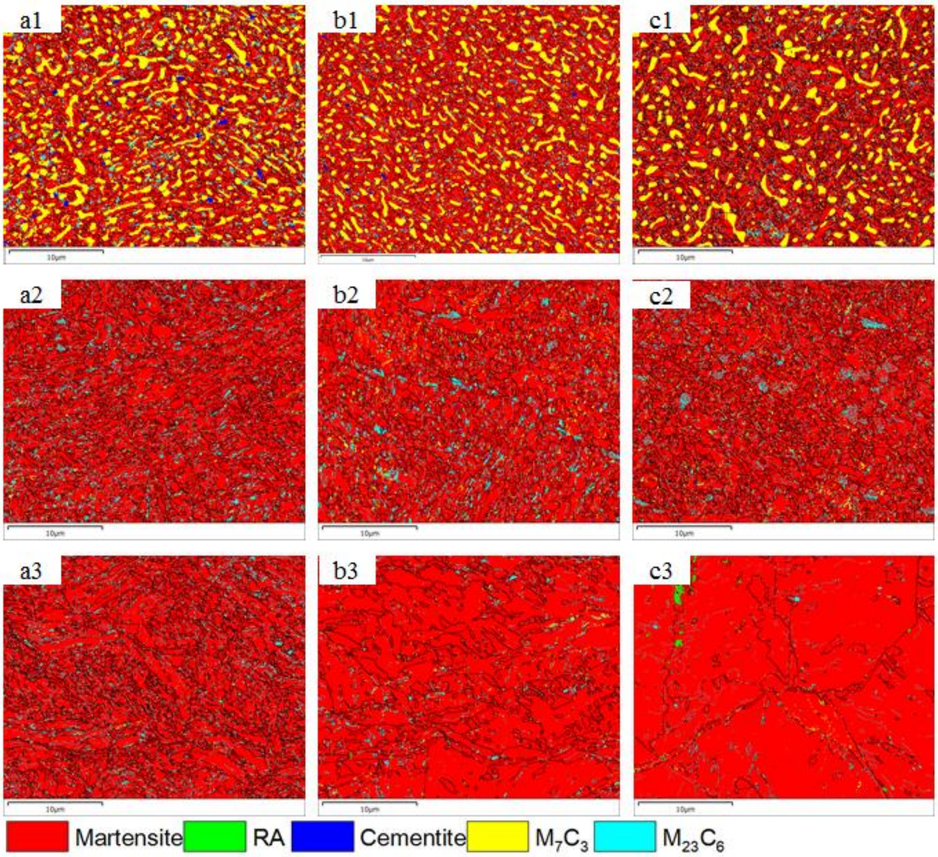

Figure 6. EBSD images of phase distribution and grain boundary superposition in the carburized zone (a1-c1), transition zone (a2-c2) and core zone (a3-c3) of the sample at different quenching temperatures: (a)1020 ° C; (b) 1050 ° C; (b) 1080 ° C.

Table 2. The content of each phase in different regions at different quenching temperatures. (%).

Phase	1020 °C			1050 °C			1080 °C		
	Carburized layer	Transition zone	Core zone	Carburized layer	Transition zone	Core zone	Carburized layer	Transition zone	Core zone
Martensite	70.3	92.1	94.9	78.1	90.7	96.8	80.1	91.5	98.3
RA	0.2	0.4	0.1	0.1	0.4	0.1	0	0.4	0.5
Cementite	1.3	0	0.1	0.6	0.4	0	0.2	0.1	0
$M_{23}C_6$	5.4	6.6	4.5	3.7	5.9	2.3	16.5	5.8	0.9
M_7C_3	22.9	0.9	0.4	17.5	2.5	0.7	3.2	2.2	0.3

3.2. Hardness Distribution

Figure 7 shows the hardness variation curves from the carburized layer to the core at different quenching temperatures. It can be observed from Figure 7 that the hardness of the samples at the three different temperatures all exhibits a gradient distribution characteristic, gradually decreasing from the surface to the core. The surface hardness of the sample is the highest, and it progressively decreases as the distance towards the core increases, eventually reaching a relatively low and stable level in the core region.

After quenching at 1020 °C and 1050 °C, the sample surfaces have high hardness levels, with peak hardness values approximately ranging from 900 to 950 HV. However, for the sample quenched at 1080 °C, the surface hardness slightly decreased, approximately 830-850 HV. In the transition zone from the surface to the core, the hardness also varied with the quenching temperature. The hardness of the specimens quenched at 1020 ° C decreases relatively gently, with a wider transition zone. However, the hardness of the specimens quenched at 1080 ° C decreases more steeply, and the transition zone is relatively narrow. The hardness of the sample quenched at 1050 °C showed intermediate behavior between the two temperatures.

The effect of different quenching temperatures on core hardness was significant. The core hardness of the samples quenched at 1020 ° C is the highest and changes little, with an average value of approximately 470-490 HV, indicating that the core microstructure is relatively uniform. The sample quenched at 1080 °C exhibited a generally lower core hardness, averaging around 270–290 HV, suggesting that although high-temperature austenitization made the core microstructure more continuous, the coarsening of the phase structure reduced hardness. In contrast, the core hardness distribution of the samples quenched at 1050 °C is uneven, with an average hardness value of approximately 300-330 HV, reflecting poor uniformity in the core microstructure.

Based on the average hardness distribution curve in Figure 7, defining a hardness of 550 HV as the effective carburized layer depth, it can be determined that for quenching temperatures of 1020 °C, 1050 °C and 1080 °C, the effective carburized layer depths of the samples are approximately 0.65 mm, 0.60 mm and 0.50 mm, respectively, which indicates that the effective carburized layer depth gradually decreases with the quenching temperature increasing.

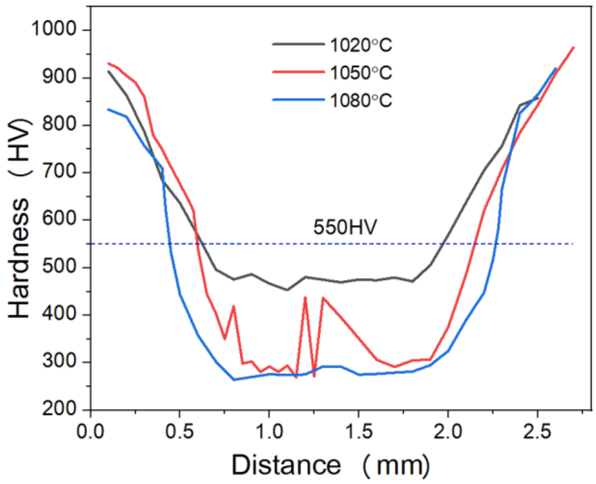

Figure 7. Hardness variation curves from the carburized layer to the core at different quenching temperatures.

3.3. Fatigue Performance Test Results

Table 3 presents the stress-number of cycles (S-N) fatigue test results for untreated initial specimens and those treated at different quenching temperatures, where Run-out indicates that the specimen does not fail after exceeding 106 cycles. Since the fatigue test data are usually discrete, statistical methods are generally required to fit these experimental results to obtain the S-N curve. Typically, the power function shown in Eqaution (2) is adopted for fitting the fatigue test results [34,35].

$$S^mN=C \tag{2}$$

where S represents stress level, N represents the number of cycles under the current stress level, and m and C represent material characteristic parameters.

Substituting the data in Table 3 into Eqaution (2) for fitting obtains the S-N curves as shown in Figure 8. The adjusted coefficients R^2 values of the fitted curves for the fatigue data of each specimen are relatively high, which are 0.91, 0.95, 0.94, and 0.91, respectively. This indicates that the S-N curve fitting accuracy for each group of specimens is high, and all curves can effectively characterize the experimental data.

By analyzing the life data at each stress level in Table 3 and Figure 8, it can be found that the life of the sample has significantly increased after heat treatment. The fatigue life of the specimens after heat treatment decreased significantly with the increase of stress level. The fatigue life of the original specimens ranged from 2.7×10^4 to 3.6×10^4 cycles at a low stress level of 203 MPa, and further decreased to a range of 7.5×10^2 to 9.0×10^2 cycles at a high stress level of 812 MPa, exhibiting the poorest fatigue resistance, as shown in Figure 8a.

After the specimens were quenched at 1020 °C, at a low stress level of 203MPa, two specimens did not fracture at 10^6 cycles, and the fatigue life of the other specimen reached 5.537×10^5 cycles. At a moderate stress level of 406MPa, the fatigue life range is 3.26×10^4 to 7.68×10^4 cycles. At a relatively high stress level of 609MPa, the fatigue life remains between 1.27×10^4 and 2.69×10^4 cycles, while at a high stress level of 812MPa, the fatigue life decreases to 4.70×10^3 to 7.80×10^3 cycles, as shown in Figure 8b.

After quenching at 1050 °C, all three specimens exhibited run-out at a low stress level of 203 MPa. When the stress level increased to 406 MPa, the fatigue life decreased to the range of 9.60×10^3 to 6.27×10^4 cycles, showing considerable scatter. At a relatively high stress level of 609 MPa, the specimen life ranged from 4.80×10^3 to 6.20×10^3 cycles. However, when the stress increased to a high level of 812 MPa, the fatigue life decreased to a range of 1.40×10^3 to 2.50×10^3 cycles, as shown in Figure 8c.

Figure 8d shows the S-N diagram of the quenching temperature of 1080 °C. Similar to specimens quenched at 1050 °C, run-out occurred in all three specimens at a low stress level of 203MPa. At a medium stress level of 406MPa, the life ranged from 1.57×10^4 to 1.97×10^4 cycles. At a relatively high stress level of 609MPa, the fatigue life is between 3.80×10^{3} and 9.20×10^{3} cycles. When the stress increased to a high level of 812 MPa, the life was reduced to a range of 3.10×10^3 to 3.80×10^3 cycles.

From Figure 8e, it can be known that at a low stress level of 203MPa, increasing the quenching temperature is beneficial for prolonging the fatigue life of the sample. However, at relatively high stress levels, raising the quenching temperature will instead lead to a reduction in fatigue. Under the condition of a constant quenching temperature, a slight increase in stress will decrease the fatigue life of the sample, indicating that the sample is sensitive to stress changes.

Figure 8f illustrated the fatigue strength of the original specimens and the specimens treated at different quenching temperatures at a given fatigue life of 10^6 cycles according to the S-N curve obtained by fitting the fatigue test data. It can be obtained that the predicted fatigue strengths are 98 MPa, 192 MPa, 183 MPa and 158 MPa, respectively. The high-cycle fatigue performance of the specimens after heat treatment was significantly improved compared with the original specimens, and it decreased with the increase of quenching temperature. The fatigue strength of the specimens was the highest at a quenching temperature of 1020 °C.

Table 3. The S-N fatigue test results for untreated initial specimens and those treated at different quenching temperatures.

	Stress(MPA)											
	203			**406**			**609**			**812**		
Initial specimens	35000	27000	36000	14600	16000	15000	1600	1400	1000	900	800	750
1020 °C	553700	Run out	Run out	76800	32600	38600	12700	14300	26900	4700	5300	7800
1050 °C	Run out	Run out	Run out	62700	9600	34300	6200	4800	6100	1400	2400	2500
1080 °C	Run out	Run out	Run out	19700	16400	15700	9200	8500	3800	3800	3100	3500

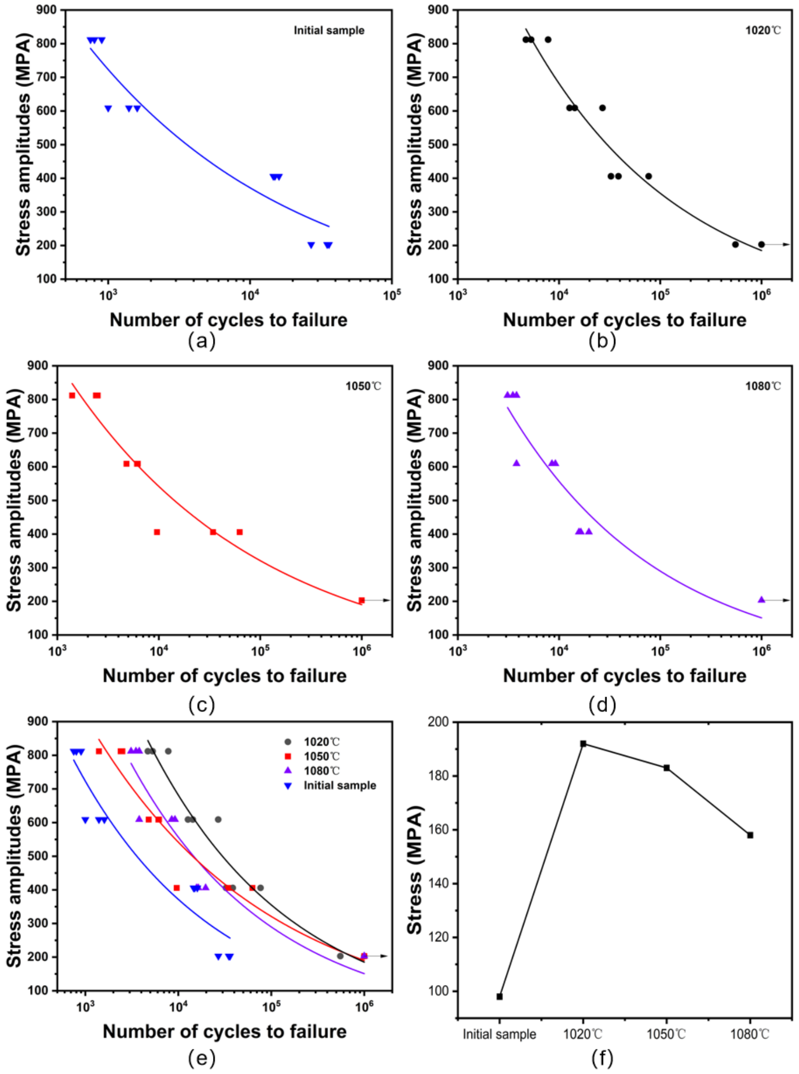

(a) (b) (c) (d) (e) (f)

Figure 8. S-N curves at different conditions: (a) the initial sample; (b) at the quenching temperature of 1020 °C; (c) at the quenching temperature of 1050 °C; (d) at the quenching temperature of 1080 °C; (e) S-N curves at different conditions; (f) the fatigue strength at different conditions at 10^6 cycles.

3.4. The Effect of Quenching Temperature on Fatigue Life

Based on the above analysis, it is evident that the fatigue performance of the specimens heat-treated is significantly superior to that of the original specimens. The main reason is that after carburizing and quenching treatment, the aviation gear steel forms a gradient microstructure from the surface to the core. The high-hardness carburized layer on the surface enhances the resistance to crack initiation, and the transition zone mitigates the property mismatch between the surface and the core, while the core provides good toughness.

The high-cycle fatigue performance of the aviation gear steel decreases with increasing quenching temperature, and the fatigue strength of the specimens is the highest at a quenching temperature of 1020 °C. This is mainly because an increase in quenching temperature will accelerate the coarsening and agglomeration of carbides in the carburized layer, promoting the refinement and dissolution of carbides in the core. At a quenching temperature of 1020 °C, the carbides in the carburized layer are relatively abundant, fine, and uniformly distributed within the matrix, while the martensite in the core is finer and less abundant compared to the other two quenching temperatures.

Furthermore, as the quenching temperature increases, the average surface hardness first increases and then decreases, while the depth of the effective carburized layer gradually reduces. At 1020 °C, the specimen surface exhibits relatively high hardness and sufficient case depth, which can effectively raise the threshold for surface crack initiation. Additionally, its core hardness is the highest with minimal fluctuation, indicating that the core microstructure is more uniform and stable. Therefore, although the surface layer of the sample quenched at 1020 °C does not have the highest hardness, the synergistic effect of surface crack resistance and core load-bearing capacity is the strongest, resulting in the highest high-cycle fatigue life.

Although the specimen quenched at 1050 °C achieves the highest surface hardness, its overall fatigue performance remains inferior to that at 1020 °C, indicating that fatigue performance is not solely governed by surface hardness. Combining SEM, EBSD, and hardness results reveals that the specimen quenched at 1050 °C has an uneven microstructure and the hardness from the surface to the core fluctuates greatly. This means that under cyclic loading, localized deformation incompatibility and stress concentration are more likely to occur in the core and transition zone. Once cracks initiate in such localized weak regions, the advantage of high surface hardness is insufficient to translate into an overall life advantage.

For the specimen quenched at 1080 °C, the core is more fully austenitized and has less residual carbides, but its surface hardness decreases, the depth of the effective hardened layer reduces, and the core hardness also declines. In other words, although high-temperature quenching improves the microstructure continuity in some areas, it weakens the dual effect of the gradient microstructure for surface strengthening and core toughness, ultimately resulting in lower fatigue strength and life compared to the specimens quenched at 1020 °C and 1050 °C.

In summary, the influence of quenching temperature on fatigue performance is a multi-factor coupling issue. As quenched at 1020 °C, the depth of the hardening layer, core toughness, microstructure refinement and gradient structure matching of the sample are the most harmonious, thereby the fatigue performance is the best. When quenched at 1050 °C, although the sample achieves the highest surface hardness, the uneven core structure weakens the overall fatigue life. When quenched at 1080 °C, coarsened microstructure, reduced effective case depth, and diminished core toughness result in poor fatigue performance of the specimens.

3.5. Fatigue Morphology and Fracture Mechanism Analysis

The fracture failure process of metallic materials mainly includes three stages: crack initiation, crack propagation and fracture failure. Under the action of cyclic loading, the damage caused by stress concentration on the surface and near the surface of the material will form crack sources, thereby leading to the initiation of fatigue cracks. By observing the macroscopic fracture morphology of the fractured specimen, the location of the fracture source and the fracture mode of the specimen can be determined. Then, the fracture mechanism of the sample was further analyzed by observing the typical fracture source locations through SEM tests.

Figure 9, Figure 10 and Figure 11 present the fracture morphology of the specimens at different quenching temperatures at a stress level of 406 MPa. Overall, the macroscopic fracture processes of the three groups of specimens are similar and no obvious crack source areas can be observed in any of them, but the crack propagation area and the final fracture area can be seen. However, there are significant differences in the local fracture morphologies corresponding to different areas of the carburized layer, transition layer and core region of the specimen, reflecting that the gradient microstructure will affect crack propagation.

Figure 9a presents the fracture morphology of the specimens quenched at 1020 °C under a stress level of 406 MPa ($N_f = 3.86 \times 10^4$). From the macroscopic fracture morphology in Figure 9a, it can be seen that the overall fracture surface of the specimen is relatively flat. However, there are still obvious differences in the roughness and flatness of the fracture surfaces among the carburized layer, transition layer, and core. The carburized layer (Region A) and the transition layer (Region B) are relatively rough, whereas the core (Regions C) is relatively flat. In addition, no obvious crack initiation zone is observed on the macroscopic fracture surface, but the crack propagation zone (Regions C) and the final fracture zone (Regions A and B) can be identified. The final fracture zone of the specimen is located in the carburized layer and the transition layer, as shown in Figures 9b, 9c, and 9d.

In the finally fractured carburized zone (Region A), a distinct “rock sugar-like” intergranular fracture feature can be observed, accompanied by local cleavage facets. The fracture mode of the specimen exhibits a mixed fracture form combining intergranular fracture and cleavage fracture. This is mainly attributed to the continuous distribution of carbides along the grain boundaries in the carburized layer. These carbides weaken the grain boundary bonding strength, making it easier for cracks to propagate along the grain boundaries, thus showing typical characteristics of intergranular brittle fracture, as shown in Figure 9b. In the finally fractured transition zone (Region B), as shown in Figure 9c, dimples and cleavage steps can be observed, which indicates a typical coexistence region of ductile microvoid aggregation and quasi-cleavage fracture. This indicates that after the crack propagates to this area, the material can, on the one hand, dissipate part of the energy through local plastic deformation, and on the other hand, undergo relatively rapid propagation along lath martensite or local interfaces. In addition, secondary cracks can be observed in this region, as shown in Figure 9d. Smooth tearing zones are visible around the cracks, while cleavage fracture traces are observed inside the cracks, indicating that this region is simultaneously affected by both local plastic tearing and brittle fracture mechanisms.

In the crack propagation zone of the core (Region C), micro-pores and dimples can be observed, indicating that a certain degree of plastic deformation occurs during the crack propagation process, as shown in Figure 9e. Additionally, some parallel and continuous fatigue striations can be observed in this region, as shown in Figure 9f, indicating that the crack did not form instantaneously but underwent a relatively stable initiation and propagation process under cyclic tensile-compressive stresses loading.

In summary, the fracture morphology characteristics of the specimen quenched at 1020 °C indicate that the core of the specimens is an important area for the initiation and early stable propagation of fatigue cracks. Cracks initiate at multiple sites in the core, gradually propagate outward, and then exhibit intergranular brittle fracture accompanied by quasi-cleavage fracture in the surface layer, finally local instantaneous fracture.

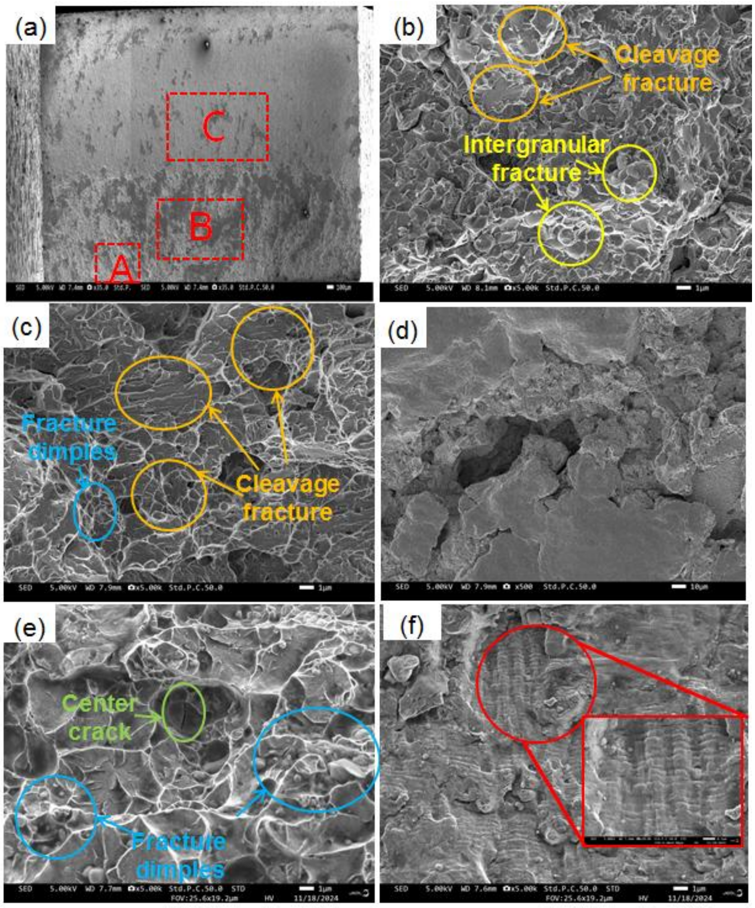

Figure 9. Fracture morphology of samples at the quenching temperature of 1020 °C with 406 MPa (N_f = 3.86 × 10^4) : (a) macroscopic morphology; (b) the carburized layer; (c) –(d) the transition layer; (e) the core; (e) fatigue striations.

Figure 10 shows the fracture morphology of the specimen quenched at 1050 °C under a stress level of 406MPa. From the macroscopic fracture morphology in Figure 10a, it can be seen that the core (Region A) and the carburized layer (Region C) are relatively rough, while the transition layer (Region B) is relatively smooth. Moreover, a large area of tearing edges can be observed in the core. Similarly, no obvious crack initiation zone is observed on the macroscopic fracture surface.

The fracture morphology of the core area (Region A) is shown in Figure 10b. In the core area, alternating fracture traces and tearing marks accompanying with cleavage plane can be observed, which indicates that brittle fractures have occurred locally in this area under higher cyclic loads， and it is also an important area for crack initiation and early propagation. Furthermore, it can be observed from Figure 10c that there is a large area of smooth tear surface in the core region, reflecting that the crack exhibited certain rapid propagation characteristics when extending through locally weak zones. This is attributed to the presence of two types of lath martensite with different sizes and spacings in the core of the specimen quenched at 1050 °C, presenting an obvious ‘bimodal’ heterogeneous microstructure. Additionally, the hardness inhomogeneity in the core is relatively large. This local mismatch between softness and hardness reduces the compatibility of plastic deformation caused by cyclic loading and make it easier to form stress concentration in the area near the core, making it easier to form stress concentrations near the core region, thereby promoting the preferential initiation and propagation of microcracks along relatively weak areas.

Figure 10d shows the fracture morphology of the transition layer (Region B). Extensive tear surfaces can also be observed in this region. Higher magnification view reveals typical fatigue striation characteristics, indicating that the propagation stage of cracks extending outward from the core occurs the region. It retains certain traces of fatigue propagation, and also exhibits a tendency for local rapid crack propagation caused by the gradient change in the internal microstructure of the material. Figure 10e presents the fracture morphology of the carburized layer. A large area of tear planes is also visible in this region, displaying obvious roughening characteristics. The high-magnification morphology map shows intergranular fracture accompanied by dimple fracture (Figure 10f), indicating that rapid fracture occurs under cyclic loading when cracks initiate near the core region and gradually propagate through the transition layer to the carburized layer, ultimately forming a final fracture zone dominated by intergranular fracture with some ductile fracture features.

In summary, for the specimen quenched at 1050 °C, the fracture characteristics reflect that the fracture mode of the aviation gear steel is mainly intergranular fracture accompanied by ductile fracture, and its fatigue behavior is highly sensitive to the inhomogeneous microstructure of the core. The 'bimodal' microstructure and uneven hardness in the core weaken the stability of crack propagation. Therefore, under the same cyclic loading conditions, its overall fatigue performance is inferior to that of the specimen quenched at 1020 °C.

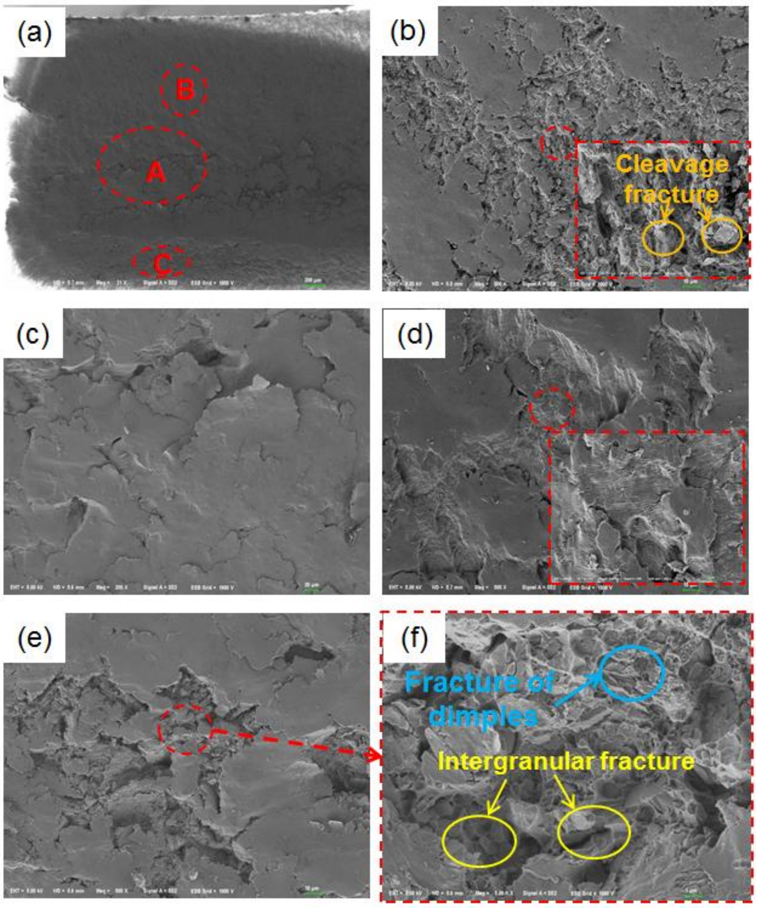

Figure 10. Fracture morphology of samples at the quenching temperature of 1050 °C with 406 MPa (Nf = 3.43 × 10^4) : (a) macroscopic morphology; (b)-(c) the core; (d) the transition layer; (e) the carburized layer; (f) high-magnification map of (e).

Figure 11 illustrates the fracture morphology of the sample quenched at 1080 °C under a stress level of 406MPa. From the macroscopic fracture morphology in Figure 11a, it can be seen that the overall fracture surface of the specimen is relatively rough, and the roughness of the carburized layer (area A) is relatively large, while the core (area C) is relatively smooth. The final fracture is located in the carburized layer. Additionally, no obvious crack initiation zone is observed on the macroscopic fracture surface as well.

Figure 11b shows the morphology of the carburized layer after fracture. The fracture surface exhibits poor flatness. At higher magnification, obvious intergranular fracture can be observed, accompanied by cleavage steps and blocky brittle spalling features. The fracture mode of the specimen is a mixed fracture pattern combining intergranular fracture and cleavage fracture. This is mainly attributed to the presence of numerous carbides distributed along the grain boundaries in the carburized layer, which weakens the grain boundary bonding strength and thus promotes crack propagation along the grain boundaries. During quenching at 1080 °C, although the number of carbides decreases, their size tends to coarser and their contours become irregular, making it easier to induce brittle delamination of the local material.

Figures 11c and 11d show the morphology of the transition layer after fracture. It can be observed that this region is dominated by cleavage fracture accompanied by intergranular fracture, indicating that under the influence of the gradient microstructure, this region exhibits a stronger tendency for rapid propagation of brittle fracture. In addition, fracture morphology features similar to those of the 1050 °C specimen can also be observed in the transition layer, namely the presence of large tear surfaces but without obvious fatigue striations, suggesting that the stable fatigue propagation characteristics in this region are weakened, and cracks propagate quickly along weak interfaces under the action of cyclic loading. The fracture morphology of the core is shown in Figures 11e and 11f. In this region, local micro-pores, dimples and tearing ridges can be observed, indicating that the outward crack propagation is accompanied by local plastic deformation and undergoes an initiation and propagation process under cyclic loading. Furthermore, fatigue striations and their propagation direction under cyclic tensile-compressive loading can be observed in Figure 11f.

Compared with the specimen quenched at 1020 °C, the residual carbides in the core are further reduced after quenching at 1080 °C, the lath martensite coarsens, and the overall hardness of the core decreases. Consequently, the load-bearing capacity of the specimen is weakened, making it easier for cracks to initiate at multiple sites in the core and propagate outward more quickly. The softening of the core, together with the retained austenite and coarsened microstructure at high temperature, jointly weakens the inhibitory effect of the gradient microstructure on crack initiation and propagation, resulting in the lowest fatigue life and fatigue strength for the specimen quenched at 1080 °C.

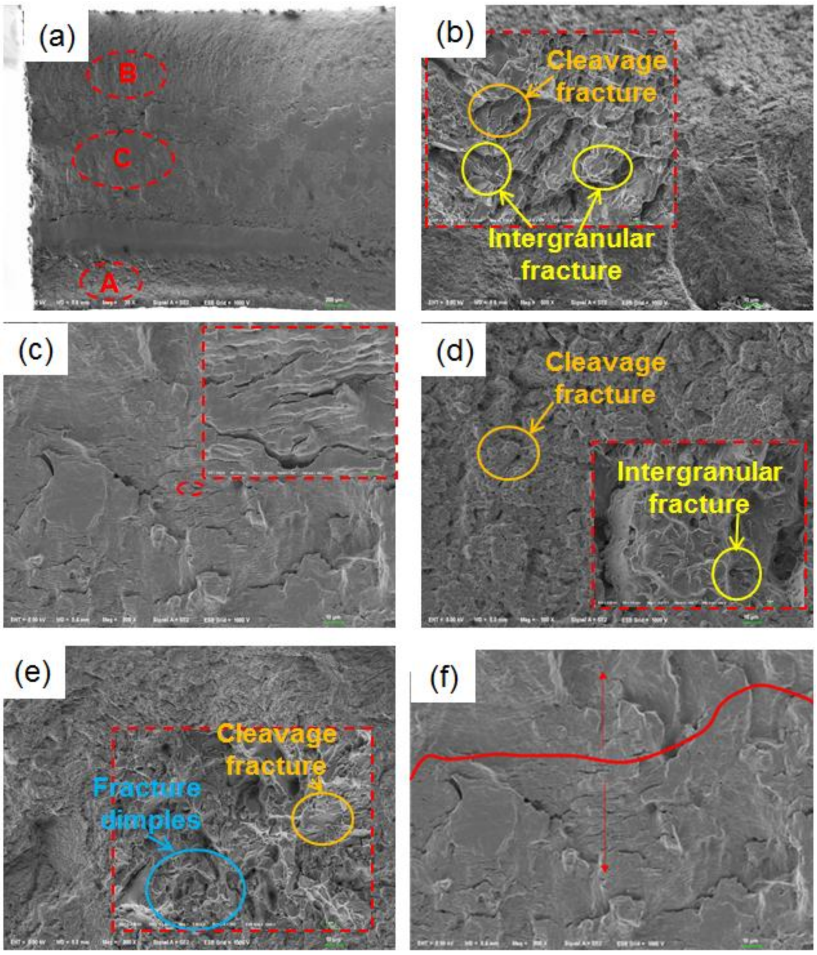

doi:10.20944/preprints202604.1274.v1

Figure 11. Fracture morphology of samples at the quenching temperature of 1080 °C with 406 MPa (N_f = 1.97 × 10^4) : (a) macroscopic morphology; (b) the carburized layer; (c) -(d) the transition layer; (e) -(f)the core.

4. Conclusions

In this work, the fatigue property of the aviation gear steel 15Cr14Co12Mo5Ni2 was investigated by means of the high-frequency fatigue test at high-temperature carburizing, and microstructure and fatigue fracture mechanism of the specimens at different quenching temperatures was analyzed in order to understand the influence of quenching temperature on its fatigue resistance. The main conclusions could be obtained as follows:

(1) After high-temperature carburizing and quenching, the aviation gear steel samples form a gradient microstructure from the carburized layer to the core. With the increase of quenching temperature, the carbide content in both the carburized layer and the core of the sample decreases, and the main carbide types are $M_{23}C_6$ and M_7C_3.

(2) The hardness of the aviation gear steel quenched at the three different temperatures all exhibits a gradient distribution characteristic, gradually decreasing from the surface to the core. The surface hardness of the samples quenched at 1020 °C and 1050 °C is higher than that of the sample quenched at 1080 °C, and the core hardness of the sample quenched at 1020 °C is the highest and the distribution is uniform. The effective carburized layer depth gradually decreases with the quenching temperature increasing, and their values are about 0.65 mm, 0.60 mm and 0.50 mm, respectively.

(3) Under the same quenching temperature, the fatigue life of the aviation gear steel decreases as the stress level increases. The fatigue life of the aviation gear steel at the three quenching temperatures is all higher than 10^6 cycles at the low stress level of 203 MPa. The fatigue life decreases with increasing quenching temperature at the stress level of 406 MPa, while at the higher stress level of 609MPa and 812was MPa, the fatigue life decreases firstly and then increases with the increasing quenching temperature. The fatigue strengths of 15Cr14Co12Mo5Ni2 gear steel at a given fatigue life of 10^6 cycles under the quenching temperature of 1020 °C, 1050 °C and 1080 °C are 192 MPa, 183 MPa and 158 MPa, respectively.

(4) At the three quenching temperatures, no obvious crack source area could be observed in the fracture morphology of the specimens and the cracks propagate outward from the core zone of the specimen, and the final fracture positions are all in the carburized layer of the specimen. As the quenching temperature increases, the crack propagation rate from the core outward accelerates. The fracture mechanism of 15Cr14Co12Mo5Ni2 gear steel at the quenching temperatures of 1020 °C was a mixed mode of intergranular and cleavage brittle fracture. At the quenching temperature of 1050 °C, the fracture mode of the aviation gear steel was mainly intergranular fracture accompanied by ductile fracture. When the quenching temperature is raised to 1080 °C, fracture mode was predominantly cleavage fracture, along with intergranular fracture and local ductile fracture.

Author Contributions: Conceptualization, W.F. and X.Z.; methodology, W.F. and Y.Z.(Yifan Zhou); validation, W.F., Y.Z. (Yifan Zhou),R.W. and Y.Z.(Yuhao Zhang); formal analysis, W.F. and Y.Z. (Yifan Zhou); investigation, Y.Z. (Yifan Zhou),R.W. and Y.Z.(Yuhao Zhang); resources, W.F. and X.Z.; data curation, Y.Z. (Yifan Zhou); writing—original draft preparation, W.F. and Y.Z.(Yifan Zhou); writing—review and editing, W.F. and Y.Z.(Yifan Zhou); visualization, W.F. and Y.Z.(Yifan Zhou); supervision, W.F. ; project administration, W.F.; funding acquisition, W.F.. All authors have read and agreed to the published version of the manuscript.

Funding: This work was financially supported by the Natural Science Foundation of China (No. 52275369), 111 Project (No. B17034) and Innovative Research Team Development Program of Ministry of Education of China (No. IRT17R83).

Institutional Review Board Statement: Not applicable.

Informed Consent Statement: Not applicable.

Data Availability Statement: The original contributions presented in this study are included in the article. Further inquiries can be directed to the corresponding authors.

Conflicts of Interest: The authors declare no conflicts of interest.

References

1. Wang, H.J.; Wang, B.; Wang, Z.D.; Tian, Y.; Misra, R.D.K. Optimizing the low-pressure carburizing process of 16Cr3NiWMoVNbE gear steel. *J. Mater. Sci. Technol* **2019**,35(7): 1218-1227.
2. Pan, Q.; Lu, L. Fatigue in metals and alloys. *Nat. Mater* **2025**,1-9.
3. Bandyopadhyay, R.; Prithivirajan, V.; Peralta, A.D.; Sangid, M.D. Microstructure-sensitive critical plastic strain energy density criterion for fatigue life prediction across various loading regimes. *Proc. R. Soc. A* **2020**,476(2236):20190766.
4. Pilgar, C.M.; Fernandez, A.M., Segurado, J. Microstructure sensitive fatigue life prediction model for SLM fabricated Hastelloy-X. *Int. J. Fatigue* **2023**,168.
5. Zhang, Y.T.; Hu, Z.; Susmel, L.; Zhang, J.; Zhang, K.; Li, Y.S.; Wang, Y.;Wei, B.C. Fatigue behaviour of a multiphase medium carbon steel: Comparison between ferrite/pearlite and tempered microstructures. *Fatigue. Fract. Eng. Mater. Struct* **2020**,43(11):2542-2549.
6. Luo, L.; Chen, Y.; Zhao, F.; Zhao, F.C.; Hua, W.F.; Song, X.; Xu, Z.Y.; Jia, Z.C. Study of the Effect of Regulating Alloying Elements and Optimizing Heat Treatment Processes on the Microstructure Properties of 20MnCr5 Steel Gears. *Lubricants* **2025**,13(5):202-202.
7. Ikuta, T.; Takahama, K.; Nojima, K.; Nishi, R.; Ono, Y.; Koide, T. Bending fatigue strength and impact strength of case-carburized gears subjected to case-depth modification by additional heat treatments. *J. MECH. SCI. TECHNOL* **2023**,37(12):6115-6122.
8. Hu, Z.W.; Mei, T.; Zou, T.; Jiang, Y.Q.; Ni, S.Y.; ZhangYu, T.N.; Wang, T.J.;Lei, L.M.; Wang, Q.Y. A comprehensive study on the low-cycle fatigue properties, damage mechanism, and microstructure evolution of 12Cr18Ni9 steel during heat treatment processes. *J. Mater. Sci* **2025**,60(26):1-20.
9. Shi, S.W.; Liu, X.M.; Xie, G.Y.; Chen, X. Enhanced cyclic stress response and low-cycle fatigue life of modified 9Cr-1Mo steel by wire-arc additive manufacturing and post-heat treatment. *Int. J. Fatigue* **2024**,184108333-.
10. Xue, Y.J.; Hui, Y.J.; Yuan, Y.; Liang, J.T.; Bai, F.X.; Xiao, B.L.; Yu, W.C.; Wang, W.Q.; Yan, Y.M. Effect of low-pressure carburizing temperature on the fatigue properties of 17Cr2Ni2MoVNb and 20Cr2Ni4A gear steels. *Mat. Sci. Eng. A-Struct* **2025**,942148728-148728.
11. Deng, Y.C.; Zhang, Y.J.; Luo, B.; Yao, X.K.; Hui, W.J.; Yin, Q.; Liu, Y.; Wu, X.L. Effect of carburizing treatment on very-high-cycle fatigue behavior of a low-carbon bearing steel. *J Mater Sci* **2025**,60(30):1-22.
12. Xue, Y.J.; Yan, Y.M.;Yu, W.C.; Dong, M.Z.; Shi, .J.;Wang, M.Q. Microstructure and fatigue properties of 17Cr2Ni2MoVNb gear steel after gas carburizing and low-pressure carburizing. *Int. J. Fatigue* **2023**,167(PA).
13. Sun, Z.D.; Hou, DB.; Li, W. Effect of Carburizing and Nitriding on Fatigue Properties of 18Cr2Ni4WA Steel in Very High Cycle Fatigue Regime. *Ann. Chim-Sci. Mat* **2021**,45(3):207-215.
14. Xiao, N.; Hui, W.J.; Zhang, Y.J.; Zhao. X.L.; Chen, Y.; Dong, H. High cycle fatigue behavior of a low carbon alloy steel: The influence of vacuum carburizing treatment. *Eng. Fail. Anal* **2020**,109104215-104215.
15. Yao, Z.H.; Dai, W.B.; Cai, B.; Li C.Y.; Zhang, H.Z.; Zhang, Y.M. Effect of Quenching Temperature on Tensile Strength and Fatigue Behavior of an EA4T Steel. *J. Mater. Eng. Perform* **2021**,30(12):9015-9028.
16. Guo, S.; Li, C.Y.; Shi, J.G.; Luan, F.J.; Song, X.Y. Effect of Quenching Media and Tempering Temperature on Fatigue Property and Fatigue Life Estimation Based on RBF Neural Network of 0.44% Carbon Steel. *Mech. Sci* **2019**,10(1):273-286.
17. Li, Y.H.; Jiang, Z.H.; Wang, P.; Li, D.Z. Effect of austenitizing temperature on isothermal quenching microstructure and mechanical properties of 52100 bearing steel. Mat. Sci. Eng. A-Struct **2024**,892146051.
18. Zhou, X.G.; Li, X.; Zeng, C.Y.; Wu, S.W.; Liu, Z.Y. Austenite Grain Growth and its Equation in the Austenitizing Process for 700 MPa Grade High-Strength Steel. *T. Indian. I. Metals* **2023**,76(11):3115-3125.
19. Li, J.R.; Zhang, C.L.; Jiang, b.; Zhou, L.Y. Effect of large-size M23C6-type carbides on the low-temperature toughness of martensitic heat-resistant steels. *J. Alloy. Compd* **2016**,248-251.

20. Wang, Y.; Xu, Y.B.; Zhang, T.Y.; Li, J.Y.; Hou, X.Y.; Sun, W.H. Effects of quenching temperature on bainite transformation, retained austenite and mechanical properties of hot-galvanized Q&P steel. *Mat. Sci. Eng. A-Struct* **2021**,822.
21. Chen, J.Z.; Zhang, B.; Zeng, L.R.; Song, Z.M.; She, Y.Y.;Zhang, G.P. Optimal Bainite Contents for Maximizing Fatigue Cracking Resistance of Bainite/Martensite Dual-Phase EA4T Steels. *Steel. Res. Int*. **2018**, 89(7):1700562.
22. An, D.Y.; Zaefferer, S. Formation mechanism of dislocation patterns under low cycle fatigue of a high-manganese austenitic TRIP steel with dominating planar slip mode. *Int. J. Plasticity* **2019**,121244-260.
23. Qiu, H.; Wang, L.; Zuo, H.; Hiraoka, k. Validity of strain-induced martensite transformation in enhancing fracture behavior of Cr–Ni weld metal at different temperatures and in different stress states. *Mat. Sci. Eng. A-Struct* **2013**,58693-99.
24. Melado, C.A.; Nishikawa, S.A.; Goldenstein, H.; Gilew.M.A.; Reed, P.A.S. Effect of microstructure on fatigue behaviour of advanced high strength ductile cast iron produced by quenching and partitioning process. *Int. J. Fatigue* **2017,**104397-407.
25. Jeddi, D.; Palin-Luc, T. Role of the martensitic microstructure in the stabilized residual stresses under cyclic loading and in the fatigue behavior of two steels. *Int. J. Fatigue* **2024**,182108168.
26. Agnani, M.; Findley, K.O.;Thompson, S.W. Effects of retained austenite and martensite microstructure on fatigue crack propagation in quenched and tempered high carbon steels. *Int. J. Fatigue* **2024**,188108529-108529.
27. Dai, W.; Shi, J.X.; Song, D.R.; He, Y.S.; Wu, B.; Li, W.D.; Zhang, H.Q.; Guo, W. Laser shock peening optimized microstructure stabilizes compressive residual stress to improve fatigue performance of high-strength aluminum alloy hole structure. *J. Mater. Sci. Technol* **2026**,24698-115.
28. Narasimhan, S.J.; Sadeghi, F.; Wang, B.; Wang, C.P. Effects of residual stress on rolling contact fatigue of ductile iron. *Int. J. Fatigue* **2025**,199109055-109055.
29. Zhao, W.D.; Liu, D.X.; Shi, H.L.; Hao, Z.Q.; Zhao, J.W. The effect of surface gradient nanostructure and compressive residual stress on fretting fatigue of A100 ultra-high strength steel by ultrasonic surface rolling process. *Int. J. Fatigue* **2025**,193108775-108775.
30. Schönbauer, B.M.; More, S.S.; Morales-Espejel, G.E.; Mayer, H. Influence of elevated temperature on the very high cycle fatigue properties of bearing steels. *Int. J. Fatigue* **2023**,176: 107847
31. Wu, Z.W.; Yang, M.S.; Zhao, K.Y. Fatigue Crack Initiation and Propagation at High Temperature of New-Generation Bearing Steel. *Metals* **2020**,11(1):25-25.
32. Han, X.H.; Chen, L.F.; Hu, X.; Hua, L.; Chai, F. Microstructure and mechanical property evolution mechanisms of 15Cr14Co12Mo5Ni2WA aviation gear steel during cold rotary forging. *J. Mater. Res. Technol* **2023**,243005-3022.
33. Burrier, H.I.; Tomasello, C.M.; Balliett, S.A.; Maloney, J.; Milam, David.L.; Ogden, W.P. Development of css-42L™, a high performance carburizing stainless steel for high temperature aerospace applications. Bearing Steels:Into the 21st Century. new Orleans,LA, USA, 01 01 1996.
34. Lai, F.Q.; Mao, K.; Cao, C.S.; Hu, A.Q.; Tu, J.X.; Lin, Y.X. Rotating Bending Fatigue Behaviors of C17200 Beryllium Copper Alloy at High Temperatures. *Materials* **2023**,16(2):815-815.
35. Hanaki, S.; Yamashita, M.; Uchida, H.; Zako, M. On stochastic evaluation of S-N data based on fatigue strength distribution. *Int. J. Fatigue* **2010**,32(3):605-609.